AGU Advances

RESEARCH ARTICLE
10.1029/2024AV001470

Were Gravity Waves or Lamb Waves Responsible for the Large-Scale Thermospheric Response to the Tonga Eruption?

Ruoxi Li[1,2,3], **Jiuhou Lei**[1,3], **Shun-Rong Zhang**[4], **Feifan Liu**[1], **Xuetao Chen**[1], **Xiaoli Luan**[1], **and Xing Meng**[1]

[1]School of Earth and Space Sciences/Deep Space Exploration Laboratory, University of Science and Technology of China, Hefei, China, [2]State Key Laboratory of Space Weather, Chinese Academy of Sciences, Beijing, China, [3]CAS Center for Excellence in Comparative Planetology/CAS Key Laboratory of Geospace Environment/Mengcheng National Geophysical Observatory, University of Science and Technology of China, Hefei, China, [4]Haystack Observatory, Massachusetts Institute of Technology, Westford, MA, USA

Peer Review The peer review history for this article is available as a PDF in the Supporting Information.

Key Points:

- The timing, amplitude, and speed of the simulated secondary GWs are consistent with the observed global thermospheric density disturbances
- These secondary GWs may cause the global-scale redistribution of thermospheric mass density
- Modeled Lamb waves exhibit smaller amplitudes at 510 km and speeds within the range of the observed thermospheric waves

Supporting Information:

Supporting Information may be found in the online version of this article.

Correspondence to:

J. Lei,
leijh@ustc.edu.cn

Citation:

Li, R., Lei, J., Zhang, S.-R., Liu, F., Chen, X., Luan, X., & Meng, X. (2025). Were gravity waves or lamb waves responsible for the large-scale thermospheric response to the Tonga eruption? *AGU Advances*, *6*, e2024AV001470. https://doi.org/10.1029/2024AV001470

Received 26 AUG 2024
Accepted 28 FEB 2025

Author Contributions:

Conceptualization: Ruoxi Li
Funding acquisition: Ruoxi Li, Jiuhou Lei
Methodology: Ruoxi Li, Jiuhou Lei
Software: Xuetao Chen
Supervision: Jiuhou Lei
Writing – original draft: Ruoxi Li
Writing – review & editing: Jiuhou Lei, Shun-Rong Zhang, Feifan Liu, Xiaoli Luan, Xing Meng

Abstract The extraordinary eruption of the Tonga volcano on 15 January 2022 lofted material to heights exceeding 50 km, marking the highest observed since the satellite era. This eruption caused significant disturbances spanning from the hydrosphere up to the thermosphere. Our recent investigation discovered the dramatic thermospheric responses at satellite altitudes. This study, however, provides physical insights into two main possible processes, secondary gravity waves (GWs) and Lamb waves, which may explain those observed large-scale thermospheric disturbances. The comparison between the simulations and observations suggests that the MESORAC-HIAMCM secondary GWs are consistent with GRACE-FO measured global-propagation thermospheric density disturbances in timing and amplitude. WACCM-X simulations suggest that the Lamb wave can reach the thermosphere as a sharp, narrow wave packet, and may contribute about 25% to the total disturbances at 510 km.

Plain Language Summary The 2022 Tonga volcanic eruption caused significant perturbations across various layers of the atmosphere, even reaching altitudes where satellites orbit. This event motivates us to investigate how energy transmits from the Earth's surface to the upper thermosphere. By combining theoretical simulations with observations, we unveil the key wave processes driving the observed thermospheric changes. When the unprecedented volcanic plumes rose into the mesosphere, they triggered primary GWs and Lamb waves. These primary GWs further generated secondary GWs that spread globally. Our analysis compared the relative contributions of GWs and Lamb waves to the excitation of large-scale global thermospheric waves. While approximately 25% of these waves in terms of magnitude could be attributed to Lamb waves, the primary contribution came from GWs.

1. Introduction

The Hunga Tonga-Hunga Ha'apai volcanic eruption on 15 January 2022, was an unprecedented event with profound impacts extending from the lithosphere to the upper atmosphere, offering a unique case for studying how surface natural hazards can extend their influence into space (Carvajal et al., 2022; Li et al., 2023; Omira et al., 2022; USGS, 2022; Wright et al., 2022). In the Earth's upper atmosphere, the ionized components (ionosphere) exhibited dramatic disturbances following the eruption, including the excitation of global-propagation ionospheric waves with various scales, as well as changes of the global ionospheric distributions (e.g., Aa et al., 2022; Amores et al., 2022; Heki, 2022; Lin et al., 2022; Liu et al., 2022; Matoza et al., 2022; Themens et al., 2022; Wright et al., 2022; S. R. Zhang et al., 2022). However, there were only a few reports on the neutral responses (thermosphere) due to the limitations of current observational techniques. Disturbances in the thermospheric temperature near 150 km, and wind spanning from 80 to 300 km altitude were detected post-eruption by satellites and ground-based radars (Aryal et al., 2023; Harding et al., 2022; Poblet et al., 2023; Stober et al., 2023). In our prior work (Li et al., 2023), we presented the first observations of the large-scale, globally propagating thermospheric waves and subsequent mass density redistributions post-eruption up to around 500 km, using thermospheric mass densities derived from Gravity Recovery and Climate Experiment Follow-On (GRACE-FO, Landerer et al., 2020) satellite accelerometer data. While these upper atmospheric responses have been detected, the mechanisms underlying the energy transmission from the epicenter to the upper atmosphere remain a topic of ongoing debate.

Various physical models have been employed to elucidate the upper atmospheric reaction to the eruption (e.g., Huba et al., 2023; Liu et al., 2023; Vadas, Becker, et al., 2023, Vadas, Figueiredo, et al., 2023; Wu et al., 2023). For instance, Liu et al. (2023) utilized Whole Atmosphere Community Climate Model with thermosphere and ionosphere eXtension (WACCM-X) to replicate the global propagation of Lamb waves' L0 and L1 modes, demonstrating consistency with ICON-MIGHTI wind observations regarding wind perturbations, wavefront tilting, and propagation speeds. Moreover, the observed large wind perturbation along the northwest coast of South America coincides with the simulated L1 mode (Poblet et al., 2023). On the other hand, Vadas, Becker, et al. (2023), Vadas, Figueiredo, et al. (2023) argued for the significance of secondary GWs in generating large-scale waves in the upper atmosphere. They employed the Model for gravity wavE SOurce, Ray trAcing and reConstruction (MESORAC) to compute primary GWs, subsequently utilizing the associated local body forces/heatings as input into the HIgh Altitude Mechanistic general Circulation Model (HIAMCM) to simulate secondary GWs. Their results showed strong agreement with ICON-MIGHTI wind measurements across four consecutive orbits, including along-track wavelengths, vertical wavelengths, vertical tilt of wavefronts, and a wide range of observed phase speeds from 100 to 600 m/s. In addition, some lower-speed waves (166–240 m/s) detected by 13 meteor radars worldwide closely matched the secondary GWs simulated by HIAMCM (Stober et al., 2024). However, the scarcity of thermospheric measurements makes it challenging to disentangle these processes and to elucidate the most important process by which momentum and energy are transmitted from the eruption to the upper atmosphere.

This paper aims to discern the fundamental physical processes governing the large-scale thermospheric responses to the eruption by integrating simulations from WACCM-X and HIAMCM with thermospheric density observations. Notably, the near-polar satellite GRACE-FO offers a broader latitudinal coverage spanning from the South Pole to the North Pole. GRACE-FO observations enable nearly continuous sampling of the thermosphere's evolution post-eruption, aiding in verifying the accuracy of simulations and unveiling the dominant underlying physical mechanisms.

2. Method

2.1. Thermospheric Density From GRACE-FO Satellite

The thermospheric mass density utilized in this study is derived from GRACE-FO accelerometer data. Launched in 2018 as a successor to the GRACE mission following its decommissioning in 2017, the GRACE-FO satellite orbits the Earth in a near-polar orbit with an altitude of approximately 510 km and a time period of 90 min, maintaining nearly constant local time at 20:20/08:20 Local Time (LT) during the Tonga eruption period (Landerer et al., 2020). Equipped with highly sensitive onboard accelerometers, GRACE-FO enables precise measurements of non-conservative forces acting on the satellite. After accounting for solar and Earth radiation pressure forces through modeling, the accelerometer data are employed to derive neutral density with a time resolution of 5 s (Li & Lei, 2021). This sampling frequency theoretically allows for a minimum detectable wavelength of 80 km given the LEO satellite speed of 7.9 km/s, according to the sampling theorem. The observed densities were normalized to 510 km for GRACE-FO to minimize the impacts of satellite altitudes (Bruinsma et al., 2004). GRACE-FO provides accurate measurement of thermospheric mass density during the eruption period, facilitating detailed detection of thermospheric responses. Note that GRACE-FO orbital densities exhibit longitudinal variability of up to 30% due to the complex influences of solar activities and lower atmospheric disturbances (Li et al., 2021, 2023). Therefore, this study appropriately focuses on large-scale thermospheric disturbances induced by the eruption.

2.2. Simulating the Secondary GWs Based on MESORAC and HIAMCM

The Tonga volcanic eruption triggered massive updrafts (plumes) reaching extraordinary altitudes of over 58 km and spanning 25–40 km in width (Vadas, Becker, et al., 2023), serving as the initial driving forces in this simulation. These plumes were identified using cloud-top brightness temperature observations from NOAA's Geostationary Operational Environmental Satellite (GOES). Subsequently, the vertical updrafts generated primary GWs. Primary GWs are those GWs directly created by the localized vertical updrafts of air triggered by the eruption (Wright et al., 2022). These eruption-induced primary GWs were reconstructed using MESORAC with the estimated updraft parameters. The local body forces (horizontal accelerations) and heatings generated where these primary GWs dissipated in the thermosphere were then utilized to drive the HIAMCM. These forces and heatings unbalanced the atmosphere, and generated secondary GWs that propagated globally. Because the secondary GWs were generated in the thermosphere, they had a wide range of horizontal speeds of 100–600 m/s. The generation and propagation of these secondary GWs were simulated using HIAMCM (see details in Vadas, Becker, et al., 2023), a high-resolution whole-atmosphere model for neutral dynamics from the surface to an altitude of about 450 km (Becker & Vadas, 2020). Note that the upper boundary is lower than GRACE-FO altitude (510 km). HIAMCM temperature variations are utilized to illustrate the evolution of the thermospheric perturbations at GRACE-FO altitude, assuming that the neutral temperature does not change between 450 and 510 km. The HIAMCM features a temporal resolution of 5 min, a horizontal resolution of 52 km, and a vertical resolution of 0.6–10 km, enabling simulation of the generation, propagation, and dissipation of secondary GWs across the entire altitude range.

2.3. Simulating the Lamb Waves Using WACCM-X

WACCM-X is a numerical model covering the entire atmosphere, from the Earth's surface to the upper thermosphere (~500 km, Liu et al., 2018). To simulate the volcanic eruption's impact on the atmosphere, 50 hPa of surface pressure was added around the volcano region in the WACCM-X model, based on barometer records. WACCM-X does not consider the effects of geomagnetic disturbances. The solar flux proxy F10.7 is set to 120, and the geomagnetic activity index Kp is set to 0.33, to isolate the impact of the volcanic eruption on the upper atmosphere. WACCM-X successfully reproduced the generation and propagation of the Lamb waves in the atmosphere (see Liu et al., 2023).

Simulation results from HIAMCM and WACCM-X are employed to explore the driving mechanisms from the lower atmospheric explosion event upward to the upper thermosphere, by comparing them with thermospheric density observations. The neutral mass density ρ is determined from $\rho = \sum_i n_i m_i$, where n_i and m_i are the number density and the relative molecular mass of each species.

3. Secondary Gravity Wave Effect

We compared post-eruption GRACE-FO density observations with HIAMCM temperature simulations to investigate the impacts of secondary GWs on the upper thermosphere. Figure 1 displays observed orbital densities from the GRACE-FO satellite and snapshots of simulated thermospheric temperature perturbations from the HIAMCM post-eruption from 06:20 to 21:00 UT.

Generally, when the polar-orbiting GRACE-FO passed over the volcano post-eruption, pairs of density-enhanced regions symmetrically appeared on both the northern and southern sides of the Tonga volcano. Density measurements from adjacent orbits suggested the generation and propagation of at least three large-scale thermospheric waves from the epicenter to the antipode (Li et al., 2023), marked by red, blue, and gray circles. On the other hand, simulations provided a comprehensive response of the global thermosphere, showing the generation and global propagation of four major thermospheric waves. These waves are clearly distinguishable, as shown in Figure 1e: At 12:30 UT, the leading wave was converging to the antipode. Meanwhile, the following wave and the third wave were crossing or heading toward the polar regions, with the fourth wave near approximately 65°S latitude.

Specifically, at 06:20 UT, about 2 hr post-eruption, Figure 1a illustrates the leading wave as two semi-circular-shaped temperature enhancements of approximately 100 K in both hemispheres around 20°N and 50°S latitude. Simultaneously, GRACE-FO was on its ascending orbit east of the volcano and experienced significant density increases when passing the simulated temperature-enhanced regions on both sides of the Tonga volcano, marked by a red circle.

From 06:20 to 14:00 UT, the leading wave propagated outward, crossed polar regions, and converged to the antipode (Figures 1a–1f). The secondary GWs have rich spectral content at this altitude, and increased from a few hundred to over 3,000 km. The simulated leading wave characteristics aligned well with GRACE-FO observations. For example, in the Southern Hemisphere, as shown in Figure 1b, a density-enhanced region observed by GRACE-FO at around 07:40 UT, near Antarctica's edge, matched the simulated leading wave both temporally and spatially. By around 09:10 UT (Figure 1c), the leading wave had propagated across the South Pole with about

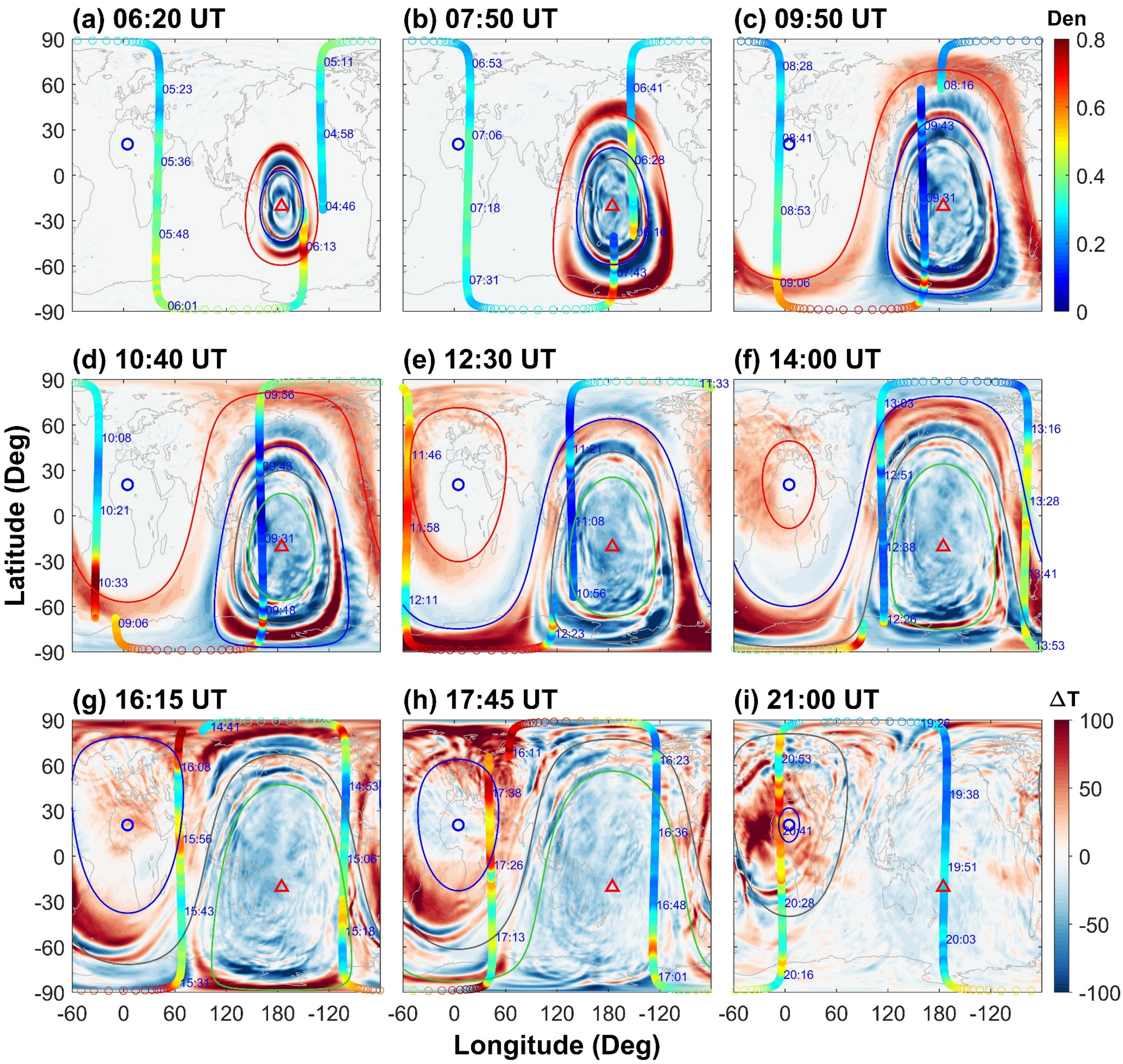

Figure 1. Observations of thermospheric densities (in units of 10^{-12} kg/m^3) along GRACE-FO trajectories post-eruption and simulated absolute changes in thermospheric temperatures (K) at 350 km using HIAMCM. GRACE-FO operated at 510 km altitude, approximately at 08:20/20:20 LT. Time epochs (in blue) of GRACE-FO are provided along the tracks. The locations of the Tonga volcano and the antipode are indicated by the red triangle and small blue circle, respectively. The propagations of the thermospheric waves are depicted by red, blue, gray, and green solid circles (lines), representing the concentrically propagating waves induced by the eruption. The wave speeds were derived from sampling fits, with sampling points intentionally chosen in areas of significantly enhanced orbital density, reflecting the satellite's passage through these waves. Note that the speed of the fourth wave (green) is estimated from the HIAMCM simulation. Absolute changes in thermospheric temperatures denote differences between the eruption and no-eruption cases. Panels (a) to (i) depict nine snapshots of the simulated evolution of thermospheric temperature post-eruption from 06:20 to 21:00 UT.

a 2,000 km wavelength and reached the South Atlantic by around 10:30 UT (Figure 1d). The large-scale density-enhanced area from approximately 60°N to 40°S resulted from GRACE-FO flying tangent to the circular wavefront (Figure 1e).

Similarly, simulations and observations showed good agreement on the arrival times for the following and the third waves at 350 km, indicating that the model accurately represents the propagation speeds. Additionally, the HIAMCM simulations show a fourth wave (green lines), and a density enhancement was also observed when

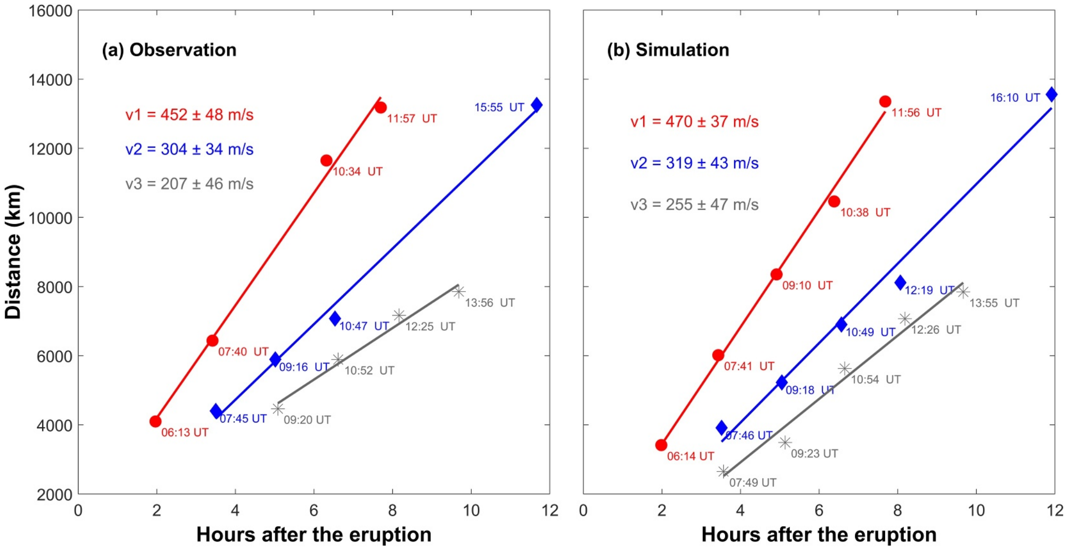

Figure 2. Comparison of thermospheric wave phase speeds estimated from GRACE-FO observations (a) and from HIAMCM simulations (b). Each data point (red circles, blue diamonds, and gray asterisks) represents the distance from the Tonga volcano to the density peaks induced by the thermospheric waves, along with the time intervals from the eruption onset of 04:15 UT to the sampling epochs. The red, blue, and gray lines correspond to the leading, following, and third waves, respectively.

GRACE-FO flew over the fourth wave at the South Polar region (Figures 1g and 1h). It is worth noting that this density enhancement may also be affected by complex geomagnetic heating effects. Given the limitations of the observational data, we will not pursue a detailed analysis of the potential fourth wave seen in the observations.

The simulated density and temperature at 350 km exhibit similar evolution characteristics (not shown) and thus we only show the simulated temperatures in Figure 1. If the thermospheric densities were extended from the simulations at 350 km to 510 km, they exhibit similar evolutionary characteristics to those at 350 km, given the thermal structure of the upper atmosphere. It should be noted that each snapshot showcases the simulated global distribution of thermospheric temperature changes at a specific moment (UT time on the upper left corner of each panel). The orbital density, on the other hand, reflects observations recorded within 1.5 hr immediately preceding that instant. Consequently, a meaningful comparison between observations and simulations should be made when the observation times (UT times in blue on the right side of the GRACE-FO trajectory) are close to the snapshot time. The supplementary Movie S1 provides a more vivid representation.

GRACE-FO experienced density enhancements each time it passed through these waves, providing samplings of these waves. We utilized the locations and the occurrence times of those density enhancements to linearly fit and estimate the wave speeds. Similarly, speeds were estimated from HIAMCM simulations. Figure 2a displays the estimated speeds from GRACE-FO observations: 452 m/s for the leading wave (red), 304 m/s for the following wave (blue), and 207 m/s for the third wave (gray). Simulations reveal comparable speeds of 470, 319, and 255 m/s for the corresponding waves, albeit slightly faster than the observations (Figure 2b). There are large uncertainties in the fitted phase speeds, likely due to the limited sampling. The GRACE-FO satellite completes an orbit around the Earth every 1.5 hr, acquiring sampling points only when passing through these thermospheric fluctuations. Additionally, the satellite's trajectory may intersect or tangentially touch the wavefront, introducing errors in sampling point selection.

Figure 3 offers a detailed comparison along GRACE-FO trajectories by illustrating both simulated (Figures 3a and 3b) and observed (Figures 3c and 3d) density variations. Three thermospheric waves, highlighted by red, blue, and gray shaded rectangles, show a strong alignment between the simulated and observed waves. The upper boundary is approximately 350 km in this case, with about 50% of simulated relative changes in density at 350 km. To compare with GRACE-FO observations, we estimate the relative changes in density at 510 km (Rel_{510}) from the following equation:

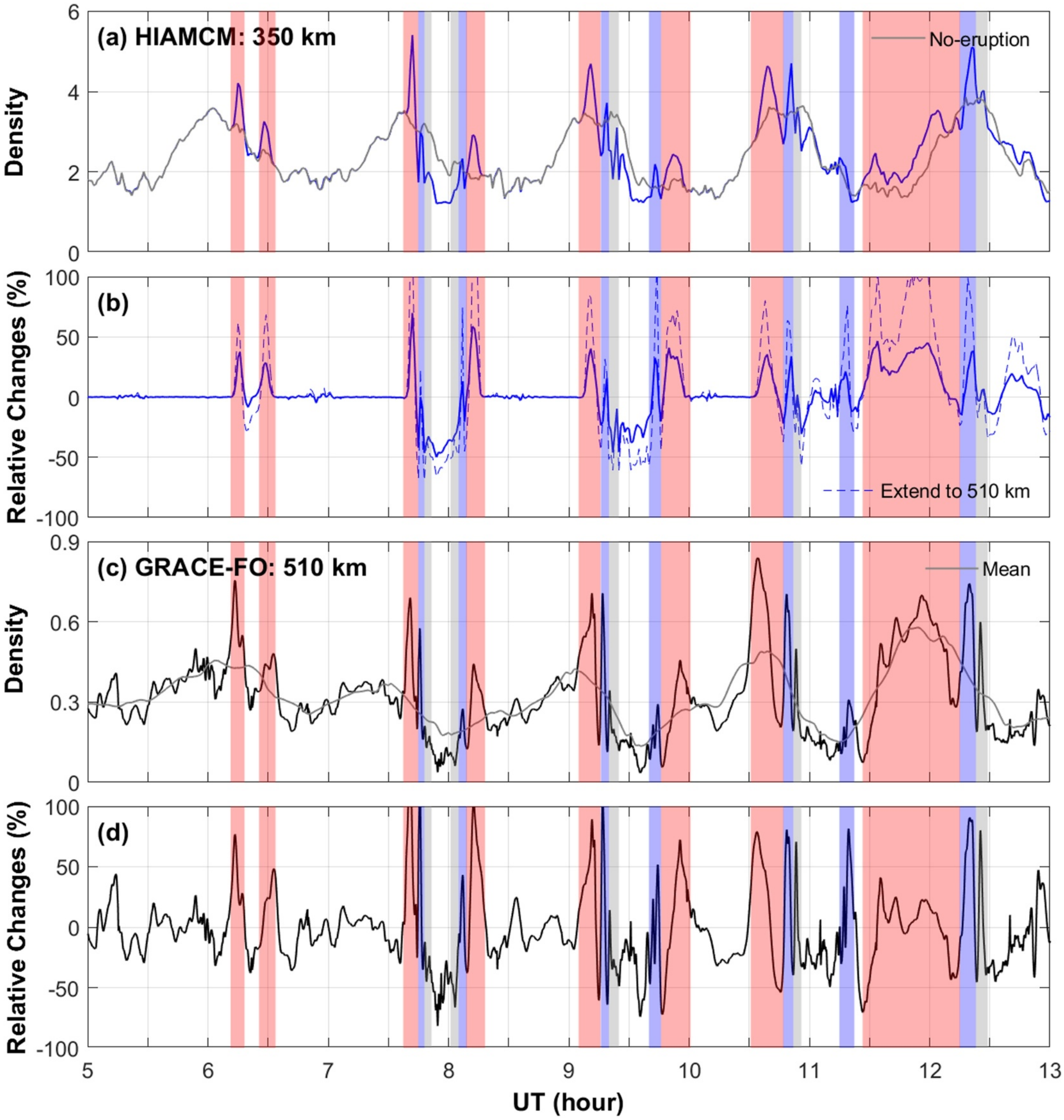

Figure 3. Thermospheric mass densities (in units of 10^{-12} kg/m^3) along the GRACE-FO trajectory and their relative changes due to the eruption, based on HIAMCM simulations and GRACE-FO observations, with respect to the running mean or the non-eruption case. Panel (a) shows the simulated thermospheric mass densities at 350 km from HIAMCM under eruption conditions (blue line) and non-eruption conditions (gray line). Panel (b) illustrates the relative change (in %) in densities between the eruption and non-eruption cases at 350 km (blue line) and the relative change extended to 510 km at GRACE-FO altitude (blue dotted line). Panel (c) presents the thermospheric mass densities from GRACE-FO (black line). A 15-min moving average is also provided for reference, corresponding to about 7,000 km based on the satellite's speed of 7.9 km/s (gray line). Panel (d) depicts the relative change in densities between the GRACE-FO observations and the moving average. The three thermospheric waves are highlighted by red, blue, and gray shaded rectangles.

$$Rel_{510} = \left(\frac{\rho_{E350} e^{\frac{-\delta h}{H_{E510}}}}{\rho_{350} e^{\frac{-\delta h}{H_{510}}}} - 1 \right) \times 100\%$$

where, ρ_{E350} and ρ_{350} represent density at 350 km under the eruption and non-eruption conditions, respectively. H_{E510} and H_{510} are the scale heights at 510 km under the two conditions. $\delta h = 160$ km represents the altitude difference (between 510 and 350 km). The atmospheric temperatures at 510 km are assumed to be the same as those of the HIAMCM simulation at 350 km. Based on the hydrostatic law, the increase in neutral temperature during the eruption leads to an increase in scale heights. Consequently, the cumulative effect of scale height

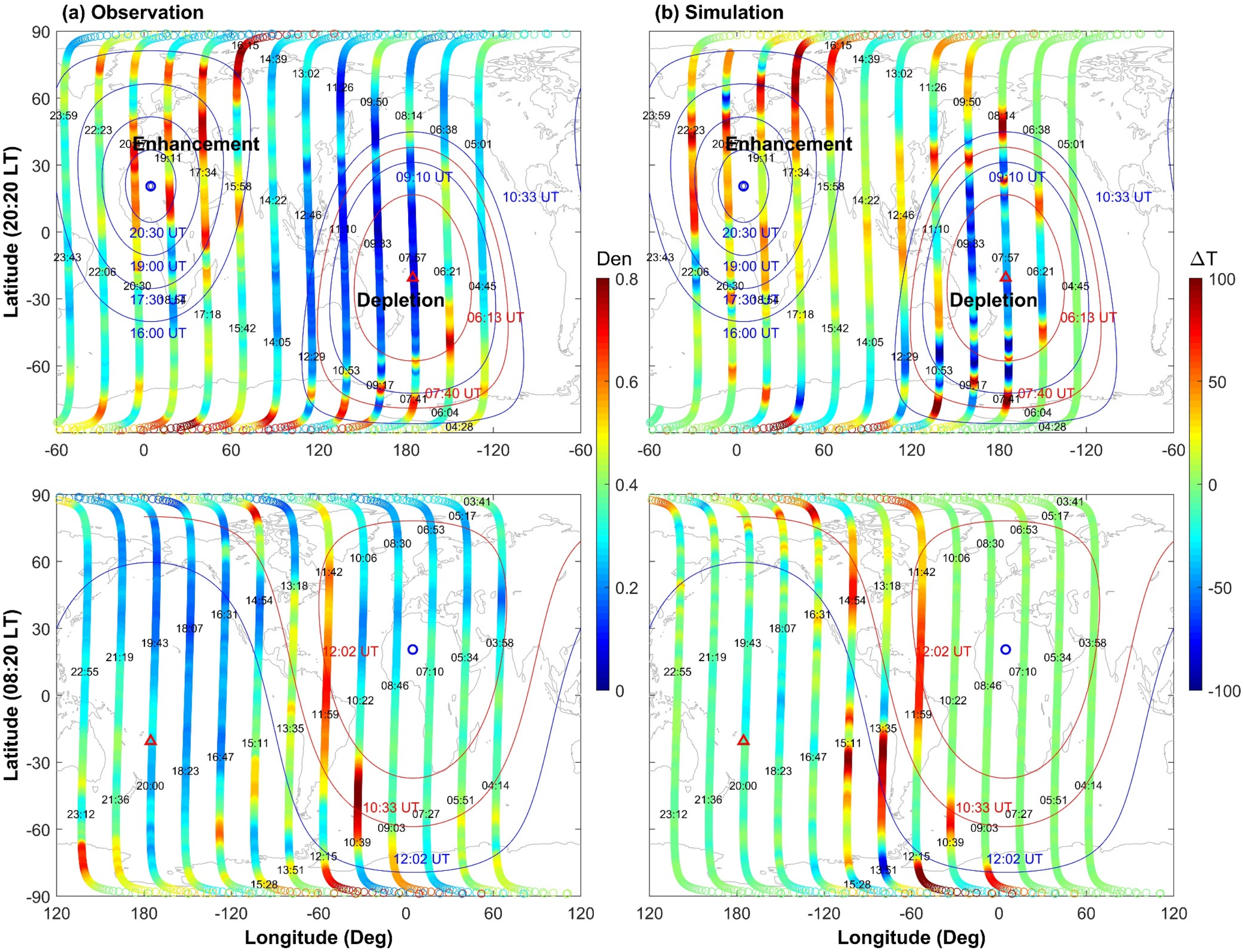

Figure 4. Observed thermospheric mass densities (in units of 10^{-12} kg/m^3) along successive GRACE-FO orbits (a), alongside the absolute changes in thermospheric temperatures (K) from HIAMCM along corresponding GRACE-FO trajectories (b) on 15 Jan. 2022. The Tonga volcano and antipode locations are denoted by a red triangle and a small blue circle, respectively. The red and blue solid circles (lines) represent the observed first and second thermospheric waves at different times, with corresponding UT times labeled near the curves. GRACE-FO orbits are categorized into dusk-side (20:20 LT) and dawn-side (08:20 LT) orbits. Densities on the dusk and dawn sides are presented in the upper and lower columns of panel (a), respectively. Panel (b) follows a similar format but displays the simulated temperature perturbations at 350 km.

variations between the heat source and the given altitude causes a greater increase in the relative change of upper thermospheric density at a higher altitude (see Lei et al., 2010). The relative changes in density at 510 km, shown by the dotted blue line in Figure 3b, are approximately 100% in response to the eruption, which is generally consistent with the GRACE-FO observations (black line in Figure 3d). The horizontal wavelength increases as the waves propagate. The dramatic increase in horizontal wavelength with radius is consistent with the behavior of GWs excited by a point source, as described by Vadas and Azeem (2021). Additionally, the secondary gravity waves can have larger speeds and wavelengths than the primary waves (Vadas & Fritts, 2002), which may explain the observed fast-moving thermospheric waves having very large horizontal wavelengths. Therefore, the simulated secondary GWs generate the most significant component of the thermospheric density disturbances, aligning in both timing and location with observations from GRACE-FO data during its global orbit.

The propagation of the thermospheric waves may cause global-scale redistribution of the thermospheric mass density. Large-scale density depletion was observed by GRACE-FO above the East Pacific Ocean around the Tonga volcano (upper left column in Figure 4a at 20:20 LT), persisting for more than 12 hr (lower column in Figure 4a). Correspondingly, significant density enhancement was detected at the antipode in North Africa and

European sectors. Simulated temperatures sampled along the GRACE-FO trajectory are displayed in Figure 4b, showing good agreement with observations.

The background temperature distribution may also contribute to the global-scale redistribution of the thermospheric mass density. Since the eruption took place during the Southern Hemisphere's summer and in the local afternoon (17:14 LT), the Tonga volcano was situated right near the region with the highest atmospheric temperatures globally. According to the HIAMCM simulation, the eruption triggered global-scale secondary GWs (involving both temperature and wind) that propagated outward from the volcano, displacing the hot air masses near the volcano outward. Consequently, a low-temperature and low-density region formed around the volcano. As night approached before atmospheric temperature and density could recover, the lack of solar energy input led to a sustained lower level of atmospheric temperature and density around the volcano for more than 12 hr post-eruption. The gravity waves converged and dissipated near the antipode, leading to an increase in temperature and density in that vicinity. Subsequently, the temperature and density near the volcano began to recover during the following local morning (details can be found in the Supporting Information S1).

4. Possible Contributions of Lamb Waves

The impact of Lamb waves on the upper atmosphere is anticipated as they tunnel from the Earth's surface upward to the ionosphere and thermosphere (Francis, 1973; Liu et al., 2023; Nishida et al., 2014). We present global temperature distributions post-eruption from WACCM-X at multiple altitudes from 200 to 500 km (Figures 5a–5e) to explore the altitude dependence of Lamb amplitudes. WACCM-X and HIAMCM temperatures along the −175°W longitude at corresponding altitudes are sampled to quantify Lamb-induced (black solid lines in Figures 5f–5j) and GW-induced (blue solid lines in Figures 5f–5j) disturbances in the thermosphere. Lamb wave impacts on the thermosphere differ from gravity waves, exhibiting much smaller wavelengths (400–500 km, compared to approximately 2,000 km for secondary GWs), and greater significance at lower altitudes. At lower altitudes (200 km), Lamb waves manifest as sharp temperature peaks, reaching approximately 150 K at their maximum. As altitude increases, these peaks dissipate, while temperature valleys become more prominent. At the altitude of 500 km, Lamb waves become temperature valleys of about 20 K. According to HIAMCM simulations, secondary GWs maintain approximately 150 K amplitude at all altitudes, as indicated by the blue shadows.

On the basis of the current simulation results, WACCM-X indicates that the impact of Lamb waves on thermospheric density at the altitude of GRACE-FO is approximately 25% of the background density, as shown in Figures 6a and 6b. This impact is much smaller than that of the secondary GWs, which is about 100%. That is, Lamb waves contribute to approximately one-fourth of the density perturbations seen in the GRACE-FO data. In other words, secondary gravity waves likely play a more crucial role in driving the large-scale thermospheric waves observed by GRACE-FO.

From an observational standpoint, isolating the small Lamb wave signal from the large-scale thermospheric disturbances at GRACE-FO altitudes (~500 km) based solely on GRACE-FO data is challenging. The difficulty arises because Lamb wave amplitudes and wavelengths are smaller than those of secondary GWs at these altitudes. Moreover, the typical longitudinal variations in GRACE-FO orbital densities, which are influenced by complex factors such as solar activities and lower atmospheric disturbances (Li et al., 2021, 2023), complicate the attribution of small-scale disturbances to Lamb waves, necessitating more comprehensive observational evidence. It should be mentioned that although gravity waves may dominate thermospheric density, this does not necessarily imply that the same conclusion holds for the ionospheric response to the eruption. The amplitude of Lamb waves is more significant at lower altitudes, being almost comparable to gravity waves at 200 km (Figure 5j). Therefore, Lamb waves may play a more important role in the ionosphere through the E-region wind dynamo mechanism. Finally, it is worth noting that the WACCM-X simulations used in this study, with a highly simplified wave source (a step function change in surface pressure at Tonga), may lead to uncertainties in estimating the wave amplitudes, while the "body force" in HIAMCM provides a more robust wave source. As a result, the exact extent of the Lamb wave impact on the thermospheric density remains uncertain.

It should be noted that a moderate geomagnetic storm occurred on January 14, one day before the Tonga eruption, with a geomagnetic activity index Kp maximum of 5.7 and an Auroral Electrojet (AE) index approaching 1,500 nT, as shown in Figure 7. From approximately 12:00 to 24:00 UT on January 15, the geomagnetic activity indices remained disturbed, with the AE maximum around 1,200 nT. The solar flux proxy F10.7 index ranged between 110 and 120 from January 14 to 16, indicating relatively high solar radiation intensity. Although the

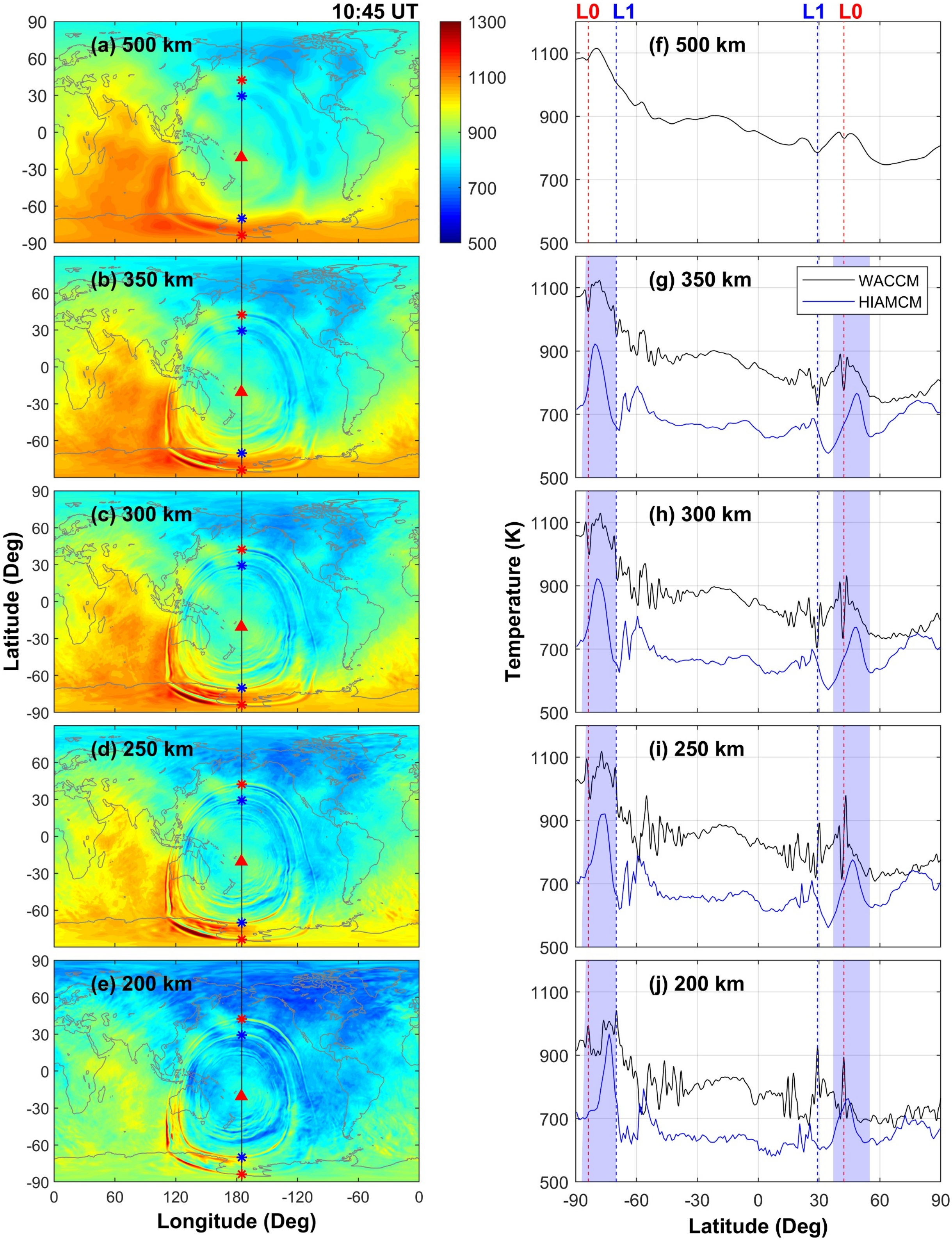

Figure 5. Global temperature distributions from WACCM-X at 200, 250, 300, 350, and 500 km at 10:45 UT (a–e). The Lamb L0 and L1 modes are sampled along the −175°W longitude (black solid lines) and are depicted by the red and blue asterisks. Panels (f) to (j) present temperatures from WACCM-X (black solid lines) and HIAMCM (blue solid lines) along the −175°W longitude. The dotted red and blue lines represent the latitudes of Lamb L0 and L1 modes corresponding to panels (a–e). The blue shadings indicate the secondary GW-induced thermospheric disturbances with a speed similar to that of the Lamb wave, ~300 m/s.

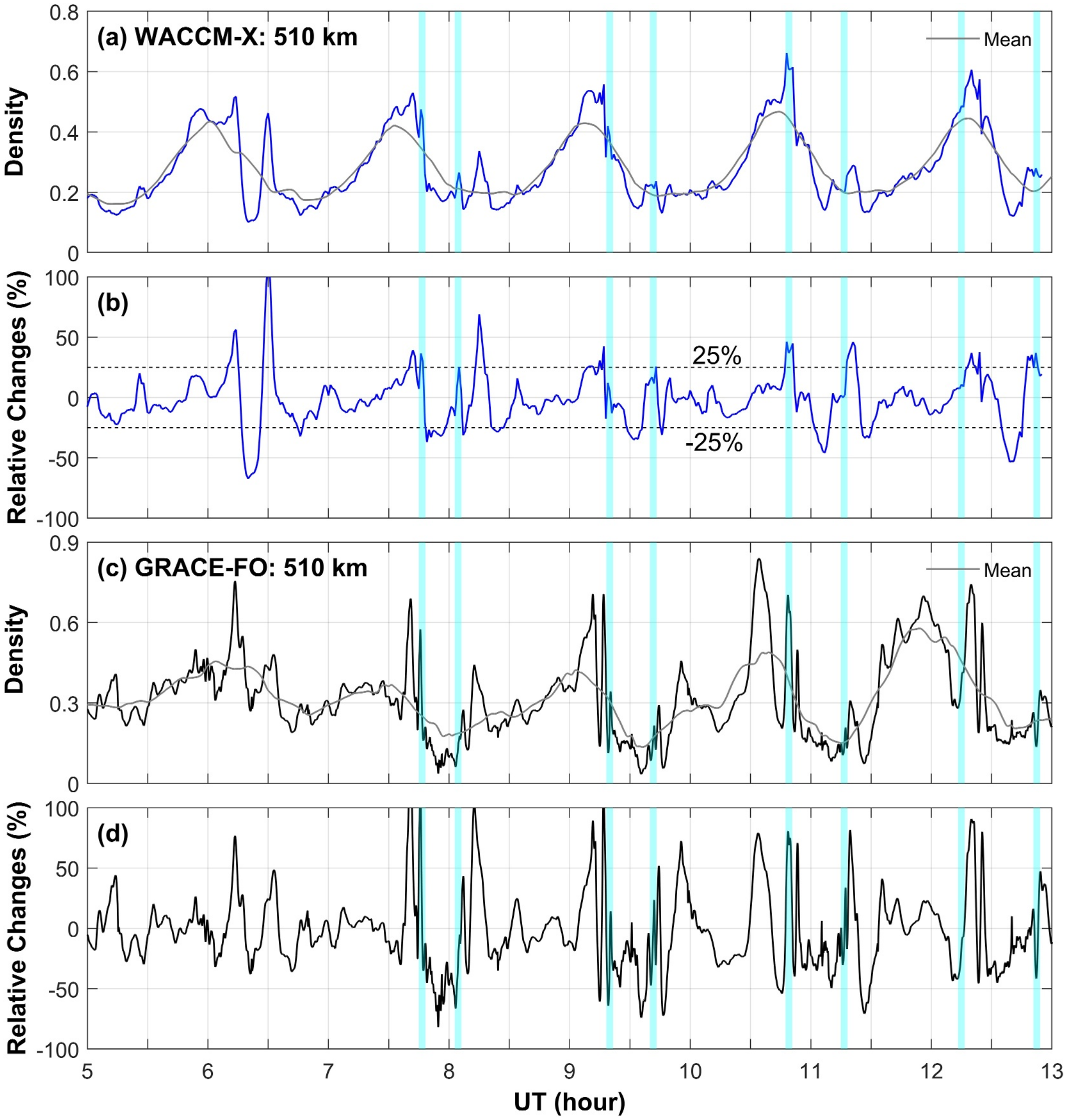

Figure 6. Similar to Figure 3, but comparing WACCM-X simulations at 510 km with GRACE-FO observations. Panel (a) presents the thermospheric mass densities from WACCM-X (blue line) and the moving average as a reference (gray line). The Lamb wave is highlighted by the shaded cyan rectangles. More details can be found in Movie S2 in the supplementary material.

geomagnetic storm could cause a significant change in the upper thermosphere, our previous simulations and statistical analyses indicate that the global-scale concentric waves observed by GRACE-FO are unlikely associated with geomagnetic storms (Li et al., 2023).

5. Conclusion

We employ two theoretical models, which incorporate the primary physical mechanisms of Lamb waves and secondary GWs that may drive thermospheric density disturbances following the Tonga eruption. To examine the effectiveness of the primary physical mechanisms, we compare two simulations with the orbital density gathered from the GRACE-FO satellite. Interestingly, simulation results demonstrate that reproducing the observed thermospheric response to volcanic eruptions is achievable solely by considering secondary gravity waves. This implies that the secondary gravity wave mechanism is likely the dominant process in generating the global-scale

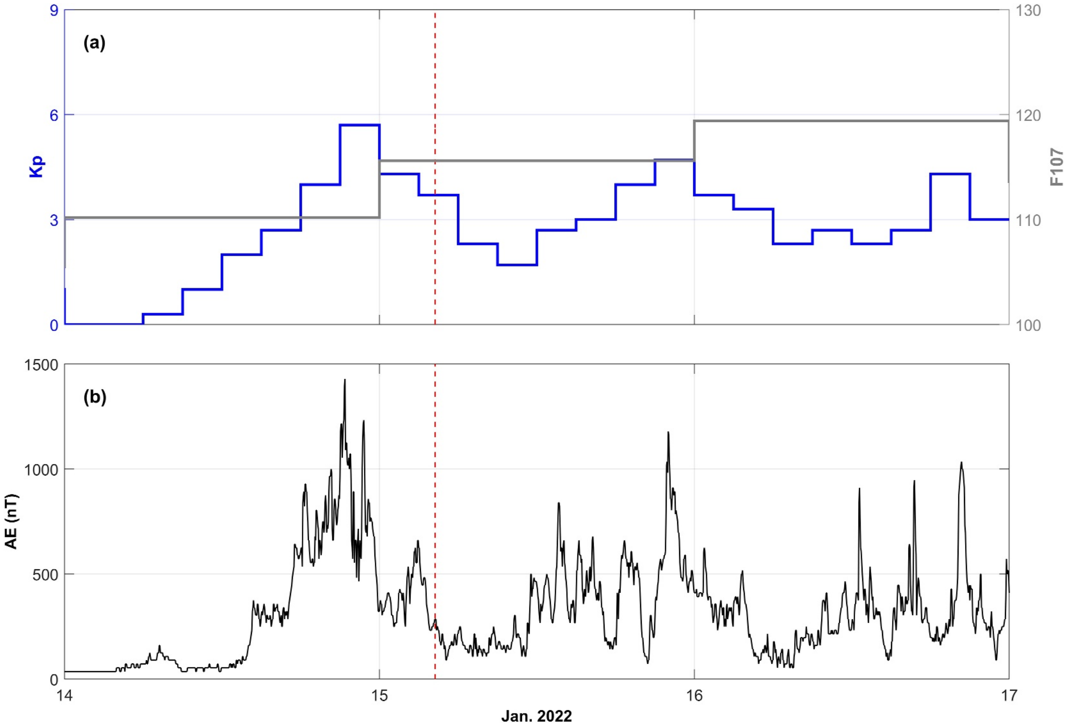

Figure 7. Variations of solar and geomagnetic activity indices from January 14 to 16, 2022. Panel (a) shows the geomagnetic activity index Kp (in blue) and the solar flux proxy F10.7 (in gray). Panel (b) displays the Auroral Electrojet (AE) index. The time of the volcanic eruption is indicated by the red dashed vertical line.

thermospheric waves. We emphasize that these thermospheric density measurements represent some large-scale perturbations during their global propagation. The Lamb wave simulations also exhibit similar propagation speeds during their global propagation, with a sharp, narrow wave packet but smaller amplitudes, approximately 25%.

Conflict of Interest

The authors declare no conflicts of interest relevant to this study.

Data Availability Statement

GRACE-FO data are obtained from the GeoForschungsZentrum (GFZ) website and are also available at Science Data Bank (ScienceDB) via https://doi.org/10.57760/sciencedb.17558 (Li, 2024). HIAMCM simulations in this paper are available at Vadas, Becker, et al. (2023); WACCM-X simulations are available at Liu et al. (2023). AE index is derived from https://wdc.kugi.kyoto-u.ac.jp/ae_realtime/index.html, and F10.7 and Kp indices are from https://omniweb.gsfc.nasa.gov/.

Acknowledgments
This work was supported by the National Natural Science Foundation of China (42188101), the B-type Strategic Priority Program of the Chinese Academy of Sciences (XDB0780000), the Project of Stable Support for Youth Team in Basic Research Field, CAS (YSBR-018), and the International Partnership Program of Chinese Academy of Sciences (Grant 183311KYSB20200003). Ruoxi Li was supported by the National Natural Science Foundation of China (42304171), the China Postdoctoral Science Foundation (2023M733363), the Joint Open Fund of Mengcheng National Geophysical Observatory (MENGO-202314), and the Project Supported by the Specialized Research Fund for State Key Laboratories. Work at MIT Haystack Observatory was supported by US NSF awards AGS-1952737, AGS-2033787, AGS-2149698, and ONR Grant N00014-23-1-2160 and N00014-24-1-2122. We acknowledge Sharon L. Vadas and H.-L. Liu for providing the simulations from HIAMCM and WACCM-X and for their useful discussions.

References

Aa, E., Zhang, S. R., Wang, W., Erickson, P. J., Qian, L., Eastes, R., et al. (2022). Pronounced suppression and X-pattern merging of equatorial ionization anomalies after the 2022 Tonga volcano eruption. *Journal of Geophysical Research: Space Physics*, *127*(6), e2022JA030527. https://doi.org/10.1029/2022JA030527

Amores, A., Monserrat, S., Marcos, M., Argüeso, D., Villalonga, J., Jordà, G., & Gomis, D. (2022). Numerical simulation of atmospheric Lamb waves generated by the 2022 Hunga-Tonga volcanic eruption. *Geophysical Research Letters*, *49*(6), e2022GL098240. https://doi.org/10.1029/2022GL098240

Aryal, S., Gan, Q., Evans, J. S., Laskar, F. I., Karan, D. K., Cai, X., et al. (2023). Tongan volcanic eruption induced global-scale thermospheric changes observed by the GOLD mission. *Geophysical Research Letters*, *50*(12), e2023GL103158. https://doi.org/10.1029/2023GL103158

Becker, E., & Vadas, S. L. (2020). Explicit global simulation of gravity waves in the thermosphere. *Journal of Geophysical Research: Space Physics*, *125*(10), e2020JA028034. https://doi.org/10.1029/2020JA028034

Bruinsma, S., Tamagnan, D., & Biancale, R. (2004). Atmospheric densities derived from CHAMP/STAR accelerometer observations. *Planetary and Space Science*, *52*(4), 297–312. https://doi.org/10.1016/j.pss.2003.11.004

Carvajal, M., Sepúlveda, I., Gubler, A., & Garreaud, R. (2022). Worldwide signature of the 2022 Tonga volcanic tsunami. *Geophysical Research Letters*, *49*(6), e2022GL098153. https://doi.org/10.1029/2022GL098153

Francis, S. H. (1973). Acoustic-gravity modes and large-scale traveling ionospheric disturbances of a realistic, dissipative atmosphere. *Journal of Geophysical Research*, *78*(13), 2278–2301. https://doi.org/10.1029/ja078i013p02278

Harding, B. J., Wu, Y. J. J., Alken, P., Yamazaki, Y., Triplett, C. C., Immel, T. J., et al. (2022). Impacts of the January 2022 Tonga volcanic eruption on the ionospheric dynamo: ICON-MIGHTI and swarm observations of extreme neutral winds and currents. *Geophysical Research Letters*, *49*(9), e2022GL098577. https://doi.org/10.1029/2022GL098577

Heki, K. (2022). Ionospheric signatures of repeated passages of atmospheric waves by the 2022 Jan. 15 Hunga Tonga-Hunga Ha'apai eruption detected by QZSS-TEC observations in Japan. *Earth Planets and Space*, *74*(1), 1–12. https://doi.org/10.1186/s40623-022-01674-7

Huba, J. D., Becker, E., & Vadas, S. L. (2023). Simulation study of the 15 January 2022 Tonga event: Development of super equatorial plasma bubbles. *Geophysical Research Letters*, *50*(1), e2022GL101185. https://doi.org/10.1029/2022GL101185

Landerer, F. W., Flechtner, F. M., Save, H., Webb, F. H., Bandikova, T., Bertiger, W. I., et al. (2020). Extending the global mass change data record: GRACE follow-on instrument and science data performance. *Geophysical Research Letters*, *47*(12), e2020GL088306. https://doi.org/10.1029/2020GL088306

Lei, J., Thayer, J. P., Burns, A. G., Lu, G., & Deng, Y. (2010). Wind and temperature effects on thermosphere mass density response to the November 2004 geomagnetic storm. *Journal of Geophysical Research*, *115*(A5), A05303. https://doi.org/10.1029/2009JA014754

Li, R. (2024). Data based on the study of "Were gravity waves or Lamb waves responsible for the large-scale thermospheric response to the Tonga eruption?" [Dataset]. *Science Data Bank*. https://doi.org/10.57760/sciencedb.17558

Li, R., & Lei, J. (2021). Responses of thermospheric mass densities to the October 2016 and September 2017 geomagnetic storms revealed from multiple satellite observations. *Journal of Geophysical Research: Space Physics*, *126*(1), e2020JA028534. https://doi.org/10.1029/2020JA028534

Li, R., Lei, J., & Dang, T. (2021). The solar eclipse effects on the upper thermosphere. *Geophysical Research Letters*, *48*(15), e2021GL094749. https://doi.org/10.1029/2021GL094749

Li, R., Lei, J., Kusche, J., Dang, T., Huang, F., Luan, X., et al. (2023). Large-scale disturbances in the upper thermosphere induced by the 2022 Tonga volcanic eruption. *Geophysical Research Letters*, *50*(3), e2022GL102265. https://doi.org/10.1029/2022GL102265

Lin, J. T., Rajesh, P. K., Lin, C. C., Chou, M. Y., Liu, J. Y., Yue, J., et al. (2022). Rapid conjugate appearance of the giant ionospheric Lamb wave signatures in the northern hemisphere after Hunga-Tonga volcano eruptions. *Geophysical Research Letters*, *49*(8), e2022GL098222. https://doi.org/10.1029/2022GL098222

Liu, H., Bardeen, C. G., Foster, B. T., Lauritzen, P., Liu, J., Lu, G., et al. (2018). Development and validation of the whole atmosphere community climate model with thermosphere and ionosphere extension (WACCM-X 2.0). *Journal of Advances in Modeling Earth Systems*, *10*(2), 381–402. https://doi.org/10.1002/2017ms001232

Liu, H. L., Wang, W., Huba, J. D., Lauritzen, P. H., & Vitt, F. (2023). Atmospheric and ionospheric responses to Hunga-Tonga volcano eruption simulated by WACCM-X. *Geophysical Research Letters*, *50*(10), e2023GL103682. https://doi.org/10.1029/2023GL103682

Liu, X., Xu, J., Yue, J., & Kogure, M. (2022). Strong gravity waves associated with Tonga volcano eruption revealed by SABER observations. *Geophysical Research Letters*, *49*(10), e2022GL098339. https://doi.org/10.1029/2022GL098339

Matoza, R. S., Fee, D., Assink, J. D., Iezzi, A. M., Green, D. N., Kim, K., et al. (2022). Atmospheric waves and global seismoacoustic observations of the January 2022 Hunga eruption, Tonga. *Science*, *377*(6601), 95–100. https://doi.org/10.1126/science.abo7063

Nishida, K., Kobayashi, N., & Fukao, Y. (2014). Background Lamb waves in the Earth's atmosphere. *Geophysical Journal International*, *196*(1), 312–316. https://doi.org/10.1093/gji/ggt413

Omira, R., Ramalho, R. S., Kim, J., González, P. J., Kadri, U., Miranda, J. M., et al. (2022). Global Tonga tsunami explained by a fast-moving atmospheric source. *Nature*, *609*(7928), 734–740. https://doi.org/10.1038/s41586-022-04926-4

Poblet, F. L., Chau, J. L., Conte, J. F., Vierinen, J., Suclupe, J., Liu, A., & Rodriguez, R. R. (2023). Extreme horizontal wind perturbations in the mesosphere and lower thermosphere over South America associated with the 2022 Hunga eruption. *Geophysical Research Letters*, *50*(12), e2023GL103809. https://doi.org/10.1029/2023GL103809

Stober, G., Liu, A., Kozlovsky, A., Qiao, Z., Krochin, W., Shi, G., et al. (2023). Identifying gravity waves launched by the Hunga Tonga-Hunga Ha′ apai volcanic eruption in mesosphere/lower-thermosphere winds derived from CONDOR and the Nordic Meteor Radar Cluster. In *Annales geophysicae*, (Vol. 41(1), 197–208). Göttingen, Germany: Copernicus Publications. https://doi.org/10.5194/angeo-41-197-2023

Stober, G., Vadas, S. L., Becker, E., Liu, A., Kozlovsky, A., Janches, D., et al. (2024). Gravity waves generated by the Hunga Tonga-Hunga Ha' apai volcanic eruption and their global propagation in the mesosphere/lower thermosphere observed by meteor radars and modeled with the High-Altitude general Mechanistic Circulation Model. *Atmospheric Chemistry and Physics*, *24*(8), 4851–4873. https://doi.org/10.5194/acp-24-4851-2024

Themens, D. R., Watson, C., Žagar, N., Vasylkevych, S., Elvidge, S., McCaffrey, A., et al. (2022). Global propagation of ionospheric disturbances associated with the 2022 Tonga volcanic eruption. *Geophysical Research Letters*, *49*(7), e2022GL098158. https://doi.org/10.1029/2022GL098158

Usgs. (2022). M 5.8 volcanic eruption-68 Km NNW of Nuku'alofa, Tonga. Retrieved from https://earthquake.usgs.gov/earthquakes/eventpage/us7000gc8r/origin/detail

Vadas, S. L., & Azeem, I. (2021). Concentric secondary gravity waves in the thermosphere and ionosphere over the continental United States on March 25-26, 2015 from deep convection. *Journal of Geophysical Research: Space Physics*, *126*(2), e2020JA028275. https://doi.org/10.1029/2020JA028275

Vadas, S. L., Becker, E., Figueiredo, C., Bossert, K., Harding, B. J., & Gasque, L. C. (2023). Primary and secondary gravity waves and large-scale wind changes generated by the Tonga volcanic eruption on 15 January 2022: Modeling and comparison with ICON-MIGHTI winds. *Journal of Geophysical Research: Space Physics*, *128*(2), e2022JA031138. https://doi.org/10.1029/2022JA031138

Vadas, S. L., Figueiredo, C., Becker, E., Huba, J. D., Themens, D. R., Hindley, N. P., et al. (2023). Traveling ionospheric disturbances induced by the secondary gravity waves from the Tonga eruption on 15 January 2022: Modeling with MESORAC/HIAMCM/SAMI3 and comparison with GPS/TEC and ionosonde data. *Journal of Geophysical Research: Space Physics*, *128*(6), e2023JA031408. https://doi.org/10.1029/2023JA031408

Vadas, S. L., & Fritts, D. C. (2002). The importance of spatial variability in the generation of secondary gravity waves from local body forces. *Geophysical Research Letters*, *29*(20), 1984. https://doi.org/10.1029/2002GL015574

Wright, C. J., Hindley, N. P., Alexander, M. J., Barlow, M., Hoffmann, L., Mitchell, C. N., et al. (2022). Surface-to-space atmospheric waves from Hunga Tonga-Hunga Ha'apai eruption. *Nature*, *609*(7928), 741–746. https://doi.org/10.1038/s41586-022-05012-5

Wu, H., Lu, X., Wang, W., & Liu, H. L. (2023). Simulation of the propagation and effects of gravity waves generated by Tonga volcano eruption in the thermosphere and ionosphere using nested-grid TIEGCM. *Journal of Geophysical Research: Space Physics*, *128*(4), e2023JA031354. https://doi.org/10.1029/2023JA031354

Zhang, S. R., Vierinen, J., Aa, E., Goncharenko, L. P., Erickson, P. J., Rideout, W., et al. (2022). Tonga volcanic eruption induced global propagation of ionospheric disturbances via Lamb waves. *Frontiers in Astronomy and Space Sciences*, *9*, 871275. https://doi.org/10.3389/fspas.2022.871275